Anion–π interactions suppress phase impurities in $FAPbI_3$ solar cells

https://doi.org/10.1038/s41586-023-06637-w

Received: 16 September 2022

Accepted: 13 September 2023

Zijian Huang[1], Yang Bai[2], Xudan Huang[3], Jiatong Li[1], Yuetong Wu[4], Yihua Chen[2], Kailin Li[1], Xiuxiu Niu[2], Nengxu Li[1], Guilin Liu[5], Yu Zhang[1], Huachao Zai[1], Qi Chen[2], Ting Lei[1], Lifen Wang[3] & Huanping Zhou[1,6] ✉

Achieving both high efficiency and long-term stability is the key to the commercialization of perovskite solar cells (PSCs)[1,2]. However, the diversity of perovskite (ABX_3) compositions and phases makes it challenging to fabricate high-quality films[3–5]. Perovskite formation relies on the reaction between AX and BX_2, whereas most conventional methods for film-growth regulation are based solely on the interaction with the BX_2 component. Herein, we demonstrate an alternative approach to modulate reaction kinetics by anion–π interaction between AX and hexafluorobenzene (HFB). Notably, these two approaches are independent but work together to establish 'dual-site regulation', which achieves a delicate control over the reaction between AX and BX_2 without unwanted intermediates. The resultant formamidinium lead halides ($FAPbI_3$) films exhibit fewer defects, redshifted absorption and high phase purity without detectable nanoscale δ phase. Consequently, we achieved PSCs with power conversion efficiency (PCE) up to 26.07% for a 0.08-cm^2 device (25.8% certified) and 24.63% for a 1-cm^2 device. The device also kept 94% of its initial PCE after maximum power point (MPP) tracking for 1,258 h under full-spectrum AM 1.5 G sunlight at 50 ± 5 °C. This method expands the range of chemical interactions that occur in perovskite precursors by exploring anion–π interactions and highlights the importance of the AX component as a new and effective working site to improved photovoltaic devices with high quality and phase purity.

Recently, metal halide perovskites (ABX_3) have emerged as promising materials for various applications, especially photovoltaics. The PCE of PSCs has rapidly increased to 26.1% (ref. 6). However, maintaining their performance during long-term operation is still challenging, especially in accelerated ageing[7], owing to the complex chemical landscape with respect to composition and phase in perovskites[1,2,8]. The resultant films present multiscale imperfections, such as point defects, component heterogeneity, undesirable residues, multiscale secondary phases and so on[3–5]. These lead to less optimal optical bandgap, adverse optoelectronic response and even material degradation[9–11]. Moreover, even in high-quality $FAPbI_3$ films for state-of-art devices, detrimental nanoscale phase impurities are discovered[12–15]. Thus, it is urgently needed to further improve the quality of perovskite materials by minimizing multiscale impurities, especially nanoscale phase impurity, which receives limited attention.

The formation of perovskite film by means of the solution process is quick with vigorous reaction and diffusion, which often involves intermediate phases[16]. Modulating precursor chemistry enables complete transformation to photoactive α phase or suppression of photoinactive δ intermediate phases. The formation of perovskite could be regarded as the reaction between AX and BX_2. In this regard, electron donors such as dimethyl sulfoxide (DMSO)[16], N-methylpyrrolidone[17], Cl^- (ref. 18), formate (Fa^-)[19] and thiocyanate (SCN^-)[20] are intensively investigated, which coordinate with electron-accepting metal cation at the B site (Pb^{2+} and Sn^{2+}) to retard nucleation and influence crystal growth substantially[19], which we refer to as the BX_2 retardants. However, commonly used electron donors such as DMSO or methylammonium chloride (MACl) only allows partial elimination of nanoscale δ-phase impurities, whereas stronger electron donors can bring in secondary phases and residuals owing to relatively strong interaction but mild crystal-growth conditions[19,21]. We proposed that, as well as merely interacting with BX_2 by using electron-donating molecules, interacting with electron-donating AX synergically by using a new type of retardants (which we refer to as the AX retardants) with electron-accepting capability may give rise to the further elaborate regulation of perovskite fabrication (as shown in Fig. 1a). However, so far, no attempts have succeeded in achieving state-of-art PSCs with the AX component as a working site for film-growth regulation. Fortunately, we find that anion–π interaction could be used as such AX retardants.

---

[1] Beijing Key Laboratory for Theory and Technology of Advanced Battery Materials, Key Laboratory of Polymer Chemistry and Physics of Ministry of Education, School of Materials Science and Engineering, Peking University, Beijing, People's Republic of China. [2] Experimental Centre for Advanced Materials, School of Materials Science and Engineering, Beijing Institute of Technology, Beijing, People's Republic of China. [3] Beijing National Laboratory for Condensed Matter Physics, Institute of Physics, Chinese Academy of Sciences, Beijing, China. [4] Beijing Key Laboratory for Theory and Technology of Advanced Battery Materials, Key Laboratory of Polymer Chemistry and Physics of Ministry of Education, College of Engineering, Peking University, Beijing, People's Republic of China. [5] School of Science, Jiangnan University, Wuxi, China. [6] Institute of Carbon Neutrality, Peking University, Beijing, People's Republic of China. ✉e-mail: happy_zhou@pku.edu.cn

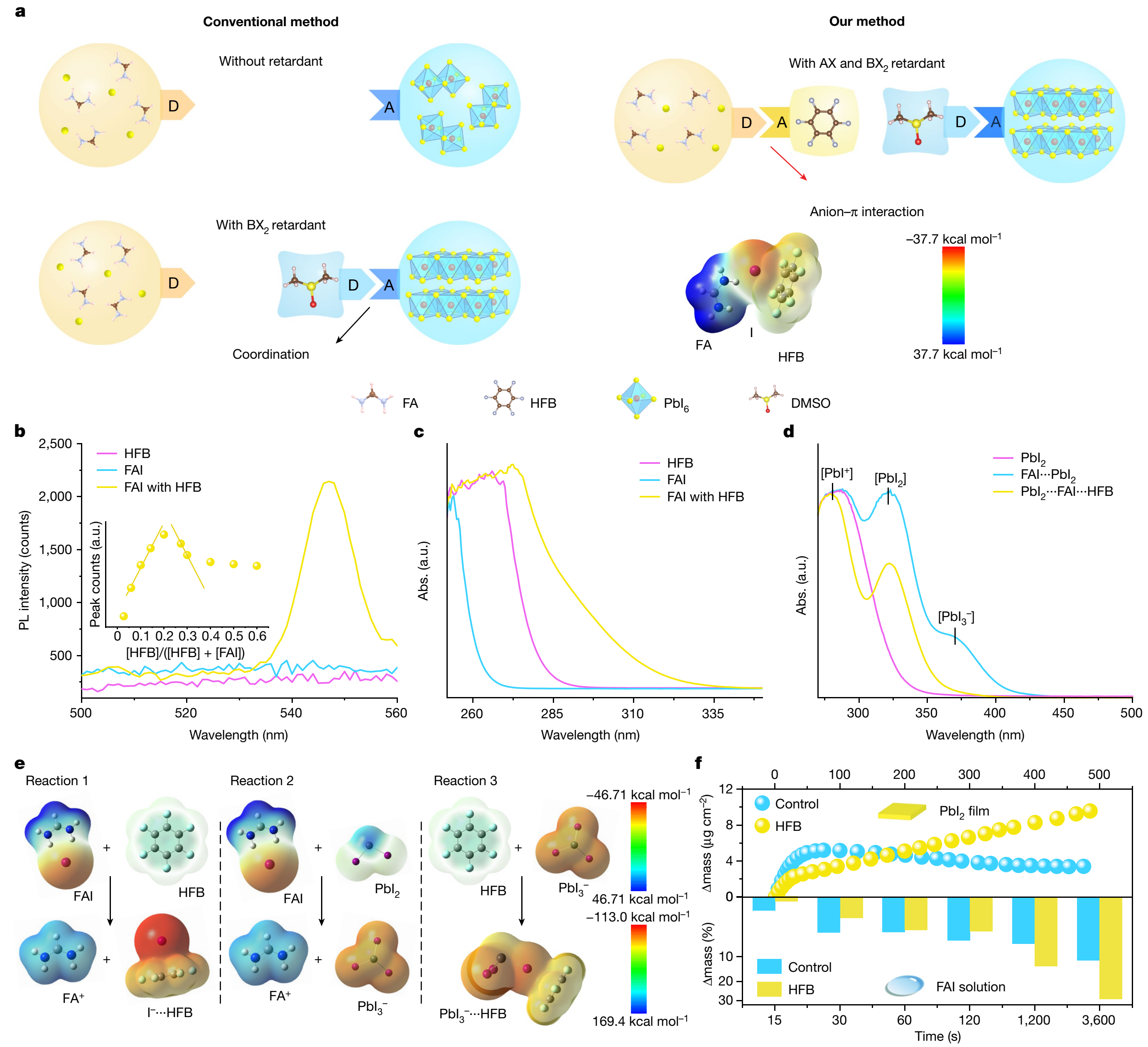

Fig. 1 | Schematic illustration and experimental investigation of anion–π interactions. a, Schematic illustration of using extra anion–π interactions as the AX retardant in perovskite processing. The colour bar ranges from −37.7 to 37.7 kcal mol^{-1}. **b**, PL spectra of FAI, HFB and mixture of FAI and HFB. The inset shows fluorescence titration of the mixture. **c**, UV–vis absorption spectra of FAI, HFB and mixture of FAI and HFB. **d**, UV–vis absorption spectra of PbI$_2$, FAI···PbI$_2$ mixture and FAI···PbI$_2$···HFB mixture. **e**, Molecular structures and corresponding Gaussian-calculated electrostatic potentials (φ) of possible structures in the FAI···PbI$_2$···HFB three-component structure, shown with the sequence reaction 1, reaction 2 and reaction 3. The colour bars range from −46.71 to 46.71 kcal mol^{-1} for electrically neutral molecules and from −113.0 to 169.4 kcal mol^{-1} for non-electrically neutral molecules. **f**, QCM-D analysis for the weight gain of PbI$_2$ films when reacted with FAI with or without HFB (upper plot) and FAI concentration decrease when reacted with PbI$_2$ films with or without HFB tested by ICP-AES (lower panel). a.u., arbitrary units.

The anion–π interaction between FAI and HFB

Anion–π interactions generally occur between an electron-deficient (π-acidic) aromatic system and an anion, and the intensity mainly relies on electrostatic forces and anion-induced polarization[22]. Earlier studies showed that the anion–π interaction between fullerene derivatives in perovskite induces n-doping of fullerene derivatives and cause passivation of defects[23,24]. With six strong electron-withdrawing fluorine atoms on the arene, HFB has an overwhelming electron deficiency with large positive quadrupole moment up to +9.5 B, which leads to stronger anion–π interaction[25]. Accordingly, the anion–π bond strength was found to be 0.53 eV (51 kJ mol^{-1}) between HFB and iodide[26], which was on the same order of magnitude as DMSO–PbI$_2$ coordination[27]. In the coordination process, BX$_2$ functions as an acceptor and retardants serve as donors; conversely, in the anion–π interaction, AX acts as a donor and HFB serves as an acceptor. Therefore, both AX and BX$_2$ components could interact with their retardants, realizing dual-site regulation of perovskite growth.

We use FAPbI$_3$ as the platform to study the anion–π interaction during film growth. Density functional theory (DFT) calculations (Fig. 1a) showed that the iodine anion interacted favourably with HFB with overlapping electron clouds, wherein the distance between iodine and

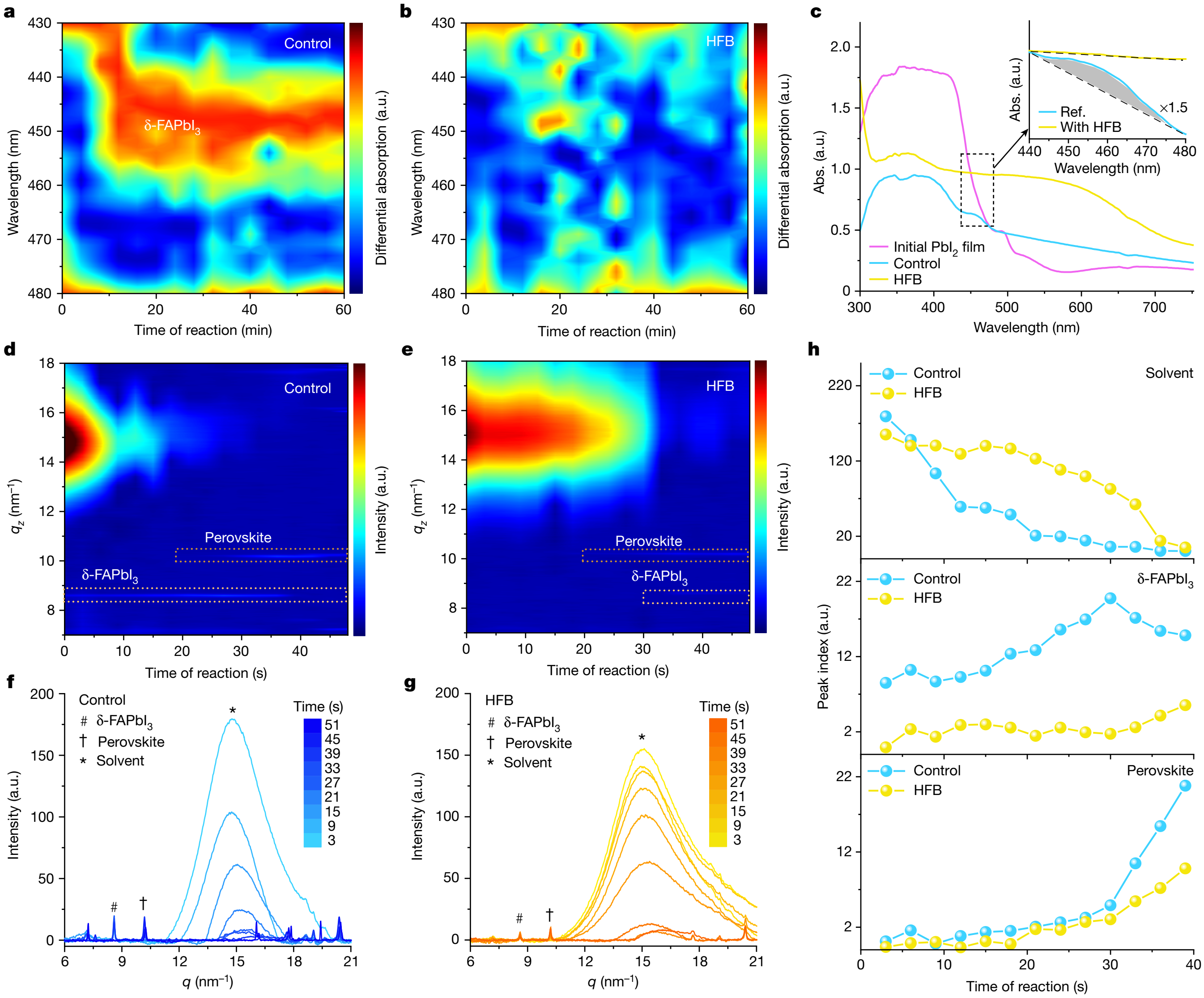

Fig. 2 | Influence of anion–π interactions on film formation. a,**b**, Differential of UV–vis absorption spectra evolution with time for lead iodide films immersed in FAI dissolved in IPA (**a**) or IPA + HFB (**b**). **c**, UV–vis absorption spectra of PbI_2 films immersed in FAI (IPA) or FAI (IPA + HFB) for 1 h. The inset shows amplified absorption between 440 nm and 480 nm. **d**,**e**, Time-resolved GIWAXS intensity maps versus q and reaction time for control (**d**) and HFB (**e**). **f**,**g**, The corresponding GIWAXS intensity profiles for control (**f**) and HFB (**g**). **h**, The time evolutions of the peak index of solvent, δ-$FAPbI_3$ and perovskite phases. a.u., arbitrary units.

carbon (3.58 Å) is shorter than the sum of their van der Waals radii. Neither HFB nor FAI/isopropyl alcohol (IPA) solution showed fluorescence at 500–560 nm (Fig. 1b). However, when HFB was introduced to the FAI/IPA solution, a new emission peak appeared at 545 nm, suggesting that a complex is probably formed. Spectrometric titration results show that the strongest emission appears when the molar ratio [HFB]/([HFB] + [FAI]) equals 0.2, implying the complex formation between 4FAI and 1HFB. We further performed ultraviolet–visible (UV–vis) absorption measurement (Fig. 1c). FAI and HFB showed absorption edges at 260 nm and 280 nm, respectively, but the HFB and FAI mixture showed a much redshifted absorption edge to 325 nm, which indicated the charge transfer between iodide and HFB. Also, in Fourier transform infrared spectroscopy (FTIR; Extended Data Fig. 1a), the skeletal vibration of FA^+ at 1,703 cm^{-1} and stretching vibration of $-NH_2$ in FA^+ at 3,355 cm^{-1} both shifted to higher wavenumber with the addition of HFB (1,722 cm^{-1} and 3,400 cm^{-1}, respectively). This is probably because the N–H···I hydrogen bond between FA+ and I− was weakened by HFB. It was also confirmed by nuclear magnetic resonance (^1H NMR) (Extended Data Fig. 1b), in which the FAI showed a prominent shift to higher field ($\Delta\delta = -0.3$ ppm) after HFB addition. The formation of FAI–HFB complex reduces the chemical potential of FAI, as tested by cyclic voltammetry measurement in Extended Data Fig. 1c.

We then studied how HFB affects the reaction between FAI and PbI_2. As shown in Fig. 1d, bare PbI_2 in dimethylformamide (DMF) showed an absorption peak at 285 nm related to PbI^+(DMF)[28]. When adding FAI to PbI_2 solution, absorption peaks related to PbI_2(DMF) and PbI_3^-(DMF) located at 325 nm and 370 nm appeared. However, on introducing HFB, the PbI_3^-(DMF) peak disappeared and the PbI_2(DMF) peak decreased considerably. This indicated that the interaction between iodine and lead could be substantially inhibited with HFB. DFT calculations were taken among possible reactions in the FAI···HFB···PbI_2 three-component system, as shown below

$$FAI + HFB \rightarrow FA^+ + [I\cdots HFB]^- \quad (1)$$

$$FAI + PbI_2 \rightarrow FA^+ + [PbI_3]^- \quad (2)$$

$$[PbI_3]^- + HFB \rightarrow [PbI_3\cdots HFB]^- \quad (3)$$

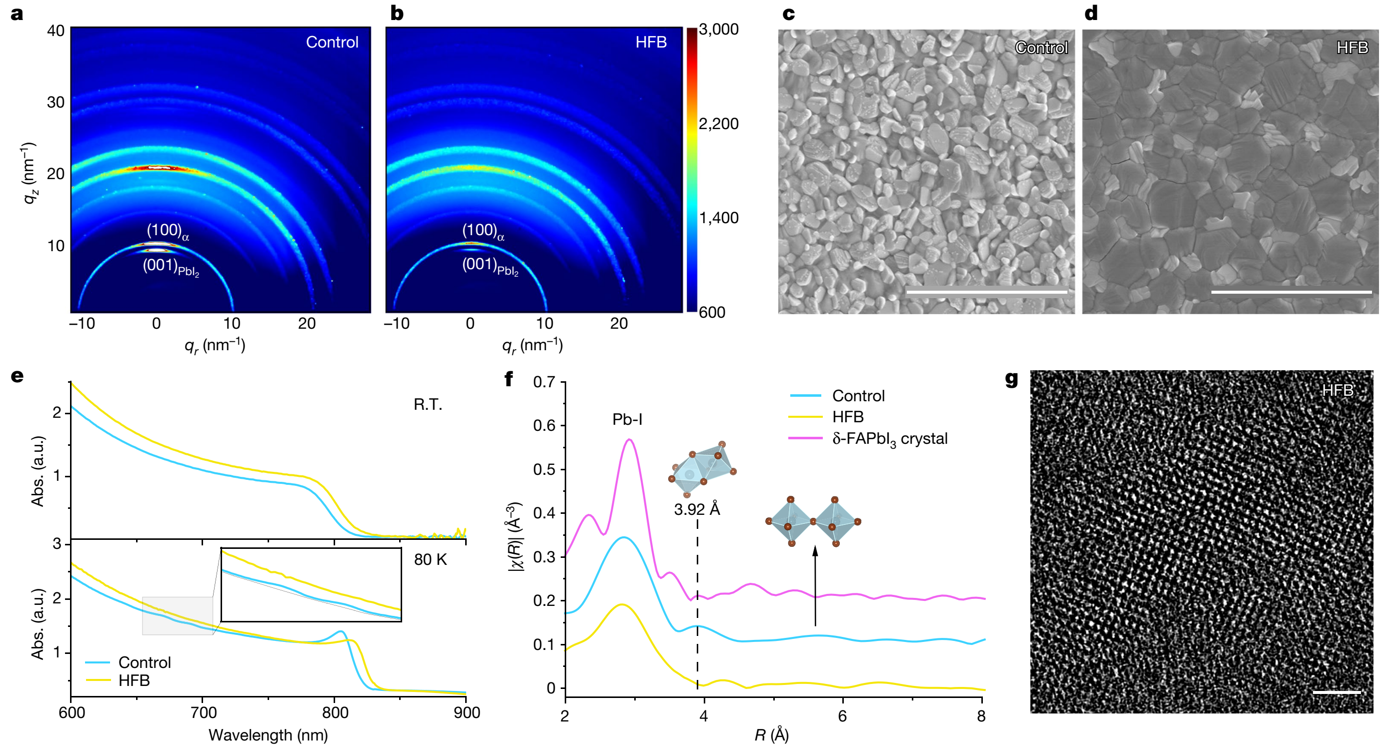

Fig. 3 | Influence of anion–π interactions on final $FAPbI_3$ perovskite films. **a**,**b**, GIWAXS profiles of the control (**a**) and HFB (**b**) perovskite films. **c**,**d**, Top-view SEM image of the control (**c**) and HFB (**d**) perovskite films. Scale bars, 5 µm. **e**, UV–vis absorption of control and HFB perovskite films at room temperature (R.T.) and 80 K (low-temperature UV–vis absorption). **f**, EXAFS of control and HFB perovskite films and δ-$FAPbI_3$ crystal. **g**, TEM of HFB perovskite on a smaller scale. Scale bar, 2 nm.

in which reaction 1 refers to the interaction between FAI and HFB and reaction 2 refers to the interaction between FAI and PbI_2. The Gibbs energy of reaction 1 (−89.7 kcal mol^{-1}) is markedly lower than that of reaction 2 (−53.1 kcal mol^{-1}), indicating that FAI has a stronger interaction with HFB rather than PbI_2. Although HFB can also interact with the product of reaction 2 ($[PbI_3]^-$), the Gibbs energy of this reaction (reaction 3) is too small (−2.51 kcal mol^{-1}) to cancel out the energy difference between reaction 1 and reaction 2. The DFT calculations were performed in gas phase (Fig. 1e) and the implicit solvent model (Extended Data Fig. 2), yielding consistent results. Thus, HFB could react with FAI to form [FAI···HFB] and retard the reaction between FAI and PbI_2.

We quantitatively study this retarding effect. The PbI_2 films immersed in FAI/IPA showed fast initial weight gain and soon reached saturation, as tested by quartz crystal microbalance with dissipation monitoring (QCM-D; Fig. 1f, upper panel), which is possibly because of the formation of δ-$FAPbI_3$ that impeded further diffusion of FAI[29]. By contrast, PbI_2 in FAI–HFB/IPA solution showed much less weight gain at the beginning but no apparent saturation. Also, 3.6% of FAI was consumed in the FAI/IPA solution, whereas only 1.2% of FAI was consumed in the FAI–HFB/IPA solution for the first 30 s, which was measured using an inductively coupled plasma emission spectrometer (Fig. 1f, lower panel). These results show that the reaction rate between FAI and PbI_2 could be effectively retarded by HFB.

As well as FAI, the UV–vis results showed that anion–π-interaction-induced polarization appears in other I^--based compounds (MAI and CsI) regardless of the cation and in different anions, such as Br^-, and even pseudohalogen anion SCN^- (Extended Data Fig. 3).

Effect of HFB on perovskite film growth

In situ UV–vis absorption measurement was implemented to investigate the $FAPbI_3$ formation process. We refer to the perovskite samples fabricated without and with HFB as the ‘control’ samples and the ‘HFB’ samples, respectively. Figure 2a,b shows the differential of in situ absorption of PbI_2·DMSO films immersed in (FAI + MACl)/IPA solution and (FAI + MACl)/(IPA + HFB) solution for 1 h, respectively. The control sample exhibited an absorption threshold at 470 nm, with the maximum differential at 450 nm (Fig. 2a,c) corresponding to δ-$FAPbI_3$, which is absent in the HFB sample (Fig. 2b,c). The absorption of the control sample was almost unchanged after the initial 10 min, although the transformation to perovskite phase in the HFB sample was slow but continuous (Supplementary Fig. 1), which suggests complete transformation from PbI_2·DMSO to perovskites.

The in situ grazing-incidence wide-angle X-ray scattering (GIWAXS) test was used to evaluate the crystallization kinetics. As shown in Fig. 2d–g, the broad scattering peak at $q \approx 15$ nm^{-1} probably originated from solvent (IPA or mixed IPA and HFB) and the sharp diffraction peaks at $q = 10.2$ nm^{-1} and 8.6 nm^{-1} represent the α-phase perovskite and 6H phase of δ-$FAPbI_3$, respectively. The solvent peak took 30 s and 12 s for the HFB and control samples, respectively, to lose half of their initial intensity. Thermal gravimetric analysis also implies more solvent residue in HFB perovskite precursor films below 70 °C (Supplementary Fig. 2). As the volatilization rate of HFB was much faster than that of IPA at room temperature (Supplementary Videos 1 and 2), the solvent residue more likely originates from the strong interaction between HFB and FAI.

In the control sample, δ-$FAPbI_3$ and α-phase perovskite was observed immediately after organic salts were deposited (Fig. 2h). The α-phase peak was located at 10.2 nm^{-1}, higher than the peak at 9.8 nm^{-1} for α-$FAPbI_3$ (ref. 30), which was attributed to the incorporation of MACl into the α-$FAPbI_3$ lattice[18]. Surprisingly, in the HFB sample, the δ-$FAPbI_3$ and α phase was absent in the first 30 s and 18 s. Different from the absorption results, some δ-$FAPbI_3$ still appeared in the HFB sample after 30 s, which might be associated with the moisture-induced degradation, along with solvent evaporation[29]. These results indicate that the addition of HFB could retard the reaction between FAI and PbI_2 at

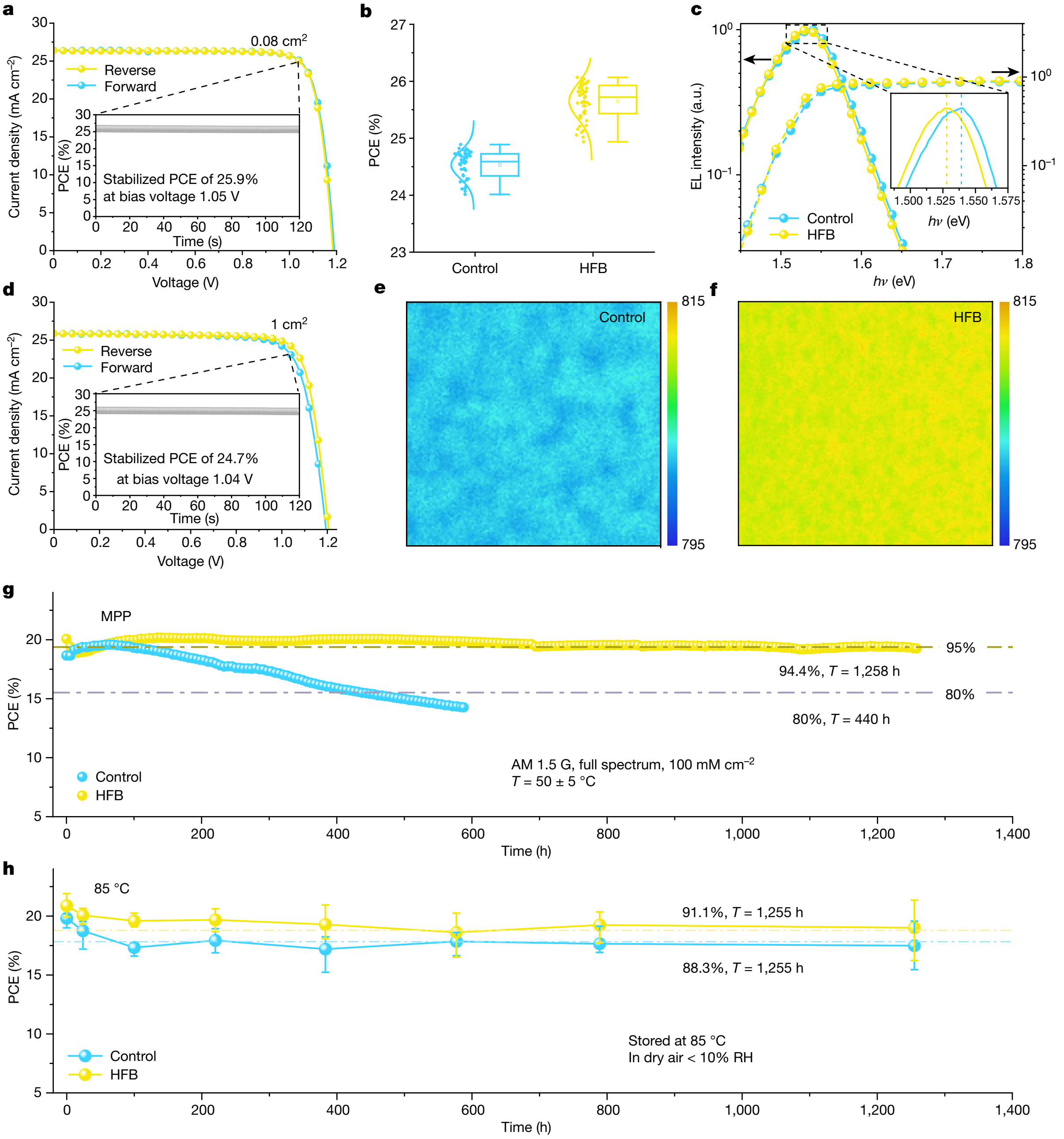

Fig. 4 | Effect of anion–π interactions on PCE and stability of PSCs. a, Reverse and forward *J*–*V* scan of FAPbI$_3$-based solar cell with HFB. **b**, Statistical analysis of control and HFB PSCs. **c**, EQE and EQE$_{EL}$ of control and HFB PSCs. **d**, *J*–*V* scan of a larger device (1.003 cm^2) with HFB. **e**,**f**, Peak position in PL mapping of control (**e**) and HFB (**f**) perovskite films. **g**, Operational stability of control and HFB PSCs. **h**, Thermal stability of control and HFB PSCs.

room temperature, which consequently suppressed the formation of δ-FAPbI$_3$ or other crystalline intermediate phase. On heating, HFB escapes from the film, which allows more direct formation of crystalline α-FAPbI$_3$ from wet film with much reduced side reaction. This dual-site regulation is different from previous methods that suppress δ-FAPbI$_3$ by forming another stable intermediate phase or accelerate sufficient transformation from δ-FAPbI$_3$ to α-FAPbI$_3$ (refs. 16,18,20).

Effect of HFB on final perovskite films

X-ray photoelectron spectroscopy (XPS) on the final HFB films (Supplementary Fig. 3) shows negligible F1s signal, indicating that HFB has escaped from the perovskite films completely after annealing. Thus, the changes of the final films probably originated from the crystallization process. The HFB sample showed narrower diffraction peaks for α-FAPbI$_3$, as measured by X-ray diffraction (XRD) (Supplementary Fig. 4) and GIWAXS (Fig. 3a,b and Supplementary Fig. 5). Besides, an increase in grain size from about 200 nm to more than 1 μm by the addition of HFB is clearly observed in the scanning electron microscopy (SEM) images (Fig. 3c,d).

Although there are no obvious diffraction signals corresponding to crystalline δ-FAPbI$_3$ observed in the control and HFB films, it is documented that nanoscale δ-FAPbI$_3$ domains (for example, nuclei) cannot be accurately detected by XRD, owing to the lack of long-range order[13,15]. Accordingly, low-temperature absorption of the control sample showed oscillatory features located around 700 nm at 80 K (Fig. 3e), implying the existence of nanoscale impurities[13]. On HFB addition, the oscillatory features disappeared. These structural differences were further confirmed using extended X-ray absorption fine structure (EXAFS) measurement. As shown in Fig. 3f, a new peak was found at 3.92 Å in *R* space for the control sample, which is consistent with the distance between the adjacent lead atoms in the face-sharing PbI_6 octahedral structure[31]. Given that the same peak at 3.92 Å in *R* space was discovered in δ-$FAPbI_3$ single crystals, we consider that this peak originated from the δ-$FAPbI_3$ structure. Notably, such a peak was absent in the HFB sample. This confirms that nanoscale impurity exists in the $FAPbI_3$ perovskite fabricated from conventional precursors ($FAPbI_3$ + MACl) and could be inhibited by the addition of HFB.

In transmission electron microscopy (TEM) measurements, δ-$FAPbI_3$ was not found in the entire region (Supplementary Fig. 6), which visually illustrates the phase purity of the HFB sample. A typical α-$FAPbI_3$ lattice was clearly seen in the enlarged image (Fig. 3g). However, the control sample was found to contain some diffraction pattern related to the δ-$FAPbI_3$ region (Supplementary Fig. 7).

Furthermore, the bandgaps of the HFB and control samples were estimated to be 1.52 and 1.54 eV, respectively, using a Tauc plot (Supplementary Fig. 8). The absorption threshold for the HFB sample reached more than 825 nm with increased absorbance. This probably originated from the reduced MA cation residue from MACl additives, as revealed by ^{1}H NMR and secondary ion mass spectroscopy (SIMS) mapping (Supplementary Figs. 9 and 10). The HFB sample also showed 2.5 times higher photoluminescence (PL) intensity and longer carrier lifetimes (2.1 μs) than control films (1.3 μs), which suggests lower defect density (Supplementary Figs. 11 and 12). A similar trend was also found for other widely adopted perovskite components with HFB, indicating that HFB can regulate the formation process of various perovskites, as shown in Supplementary Figs. 13–15.

Performance of perovskite devices with HFB

We then fabricated PSCs (FTO/SnO_2/$FAPbI_3$/spiro-OMeTAD/Au). The best HFB device (0.0831 cm^2) achieved a PCE of 26.07% in forward scan and 26.01% in reverse scan, giving 26.04% on average (Fig. 4a and Extended Data Table 1). A best stabilized power output of 25.9% was achieved. By contrast, the PCE of control PSCs achieved 24.81% in reverse scan. Statistical analyses on 100 individual devices with or without HFB were summarized. The PCE for HFB achieved 25.65% on average compared with 24.53% for the control (Fig. 4b and Supplementary Fig. 17). A certified 25.8% PCE was achieved with no hysteresis at the National Institute of Metrology, China (NIM) (Supplementary Figs. 18 and 19). The improvement of efficiency mainly comes from current density and open-circuit voltage. We determined the radiative limit for the open-circuit voltage (V_{OC}^{rad}) from the external quantum efficiency and electroluminescent spectrum (EQE-EQE_{EL}) (Fig. 4c), with 1.236 V and 1.254 V for the HFB and control samples, respectively, thus non-radiative V_{OC} loss was calculated to be 0.043 V and 0.076 V for each sequentially. The enhancement in J_{SC} is confirmed using EQE measurement (Supplementary Fig. 20). We also investigate the three following molecules by forming anion–π interactions with halogen: 2,4,6-trifluoro-1,3,5-triazine, s-tetrazine and pentafluoropyridine, which take effects similarly as HFB, as shown in Extended Data Fig. 4.

We also fabricated PSCs with larger areas (1.003 cm^2) and the best-performing device exhibited a PCE of 25.12%, with a high V_{OC} of 1.205 V in reverse scan and 24.13% in forward scan (24.63% on average), which is the highest PCE ever reported for a 1-cm^2 device so far. PL mapping of perovskite films was performed and the HFB film was found to be more uniform (Fig. 4e,f), which might be of benefit to larger-area PSCs.

The control $FAPbI_3$ films remained at only 45% of its initial absorbance on average for ten films, after ageing under humidity (relative humidity (RH) 50–60%) at room temperature (approximately 20 °C) for 72 h (Supplementary Fig. 21), although 82% of their initial absorption remained for HFB films on average. One of the best HFB films remained at 95% of its initial absorption after 120 h (Supplementary Fig. 22). We further investigated the operational stability of these PSCs by ageing them under nitrogen atmosphere, using MPP tracking with 1-sun illumination at 50 ± 5 °C with a spectral mismatch lower than 2% to AM 1.5 G (Supplementary Fig. 23). As shown in Fig. 4g, the PCE of the control PSCs decreased by 30% after 600 h, whereas the HFB devices remained at 94% of its initial efficiency after 1,258 h. We further studied their stability at 85 °C (Fig. 4h). Control PSCs retained an average of 88.3% of their initial efficiency after 1,255 h for 12 devices. Devices with HFB retained 91.8% of their initial efficiency on average for 12 devices. The enhanced heat resistance might be understood as reduced MA cation residue in HFB perovskite.

Overall, we have shown that the growth of halide perovskites can be substantially regulated by anion–π interaction with halide in the AX component, which is independently conducted but works well together with BX_2 regulation, leading to dual-site regulation. Particularly, it inhibits formation of δ-$FAPbI_3$ and reduces component residue in α-$FAPbI_3$ perovskite, which improves component and phase purity, especially without detectable nanoscale phase impurity. Furthermore, because anion–π interactions widely present between electron-deficient systems and anions, these findings and methodologies may be extended to other solution-processed compound materials with electron-donating anions.

Online content

Any methods, additional references, Nature Portfolio reporting summaries, source data, extended data, supplementary information, acknowledgements, peer review information; details of author contributions and competing interests; and statements of data and code availability are available at https://doi.org/10.1038/s41586-023-06637-w.

1. Rao, M. K. et al. Review on persistent challenges of perovskite solar cells' stability. *Sol. Energy* **218**, 469–491 (2021).
2. Mohd Yusoff, A. R. B. et al. Passivation and process engineering approaches of halide perovskite films for high efficiency and stability perovskite solar cells. *Energy Environ. Sci.* **14**, 2906–2953 (2021).
3. Chen, B., Rudd, P. N., Yang, S., Yuan, Y. & Huang, J. Imperfections and their passivation in halide perovskite solar cells. *Chem. Soc. Rev.* **48**, 3842–3867 (2019).
4. Yin, W.-J., Shi, T. & Yan, Y. Unusual defect physics in $CH_3NH_3PbI_3$ perovskite solar cell absorber. *Appl. Phys. Lett.* **104**, 063903 (2014).
5. Correa-Baena, J.-P. et al. Homogenized halides and alkali cation segregation in alloyed organic-inorganic perovskites. *Science* **363**, 627–631 (2019).
6. National Renewable Energy Laboratory (NREL). Best Research-Cell Efficiencies. *NREL* https://www.nrel.gov/pv/assets/pdfs/best-research-cell-efficiencies.pdf (2023).
7. Khenkin, M. V. et al. Consensus statement for stability assessment and reporting for perovskite photovoltaics based on ISOS procedures. *Nat. Energy* **5**, 35–49 (2020).
8. Li, W. et al. Chemically diverse and multifunctional hybrid organic–inorganic perovskites. *Nat. Rev. Mater.* **2**, 16099 (2017).
9. Ma, J.-P. et al. Defect-triggered phase transition in cesium lead halide perovskite nanocrystals. *ACS Mater. Lett.* **1**, 185–191 (2019).
10. Yuan, Y. & Huang, J. Ion migration in organometal trihalide perovskite and its impact on photovoltaic efficiency and stability. *Acc. Chem. Res.* **49**, 286–293 (2016).
11. Slotcavage, D. J., Karunadasa, H. I. & McGehee, M. D. Light-induced phase segregation in halide-perovskite absorbers. *ACS Energy Lett.* **1**, 1199–1205 (2016).
12. Frohna, K. et al. Nanoscale chemical heterogeneity dominates the optoelectronic response of alloyed perovskite solar cells. *Nat. Nanotechnol.* **17**, 190–196 (2022).
13. Wright, A. D. et al. Intrinsic quantum confinement in formamidinium lead triiodide perovskite. *Nat. Mater.* **19**, 1201–1206 (2020).
14. Macpherson, S. et al. Local nanoscale phase impurities are degradation sites in halide perovskites. *Nature* **607**, 294–300 (2022).
15. Doherty, T. A. S. et al. Stabilized tilted-octahedra halide perovskites inhibit local formation of performance-limiting phases. *Science* **374**, 1598–1605 (2021).
16. Yang, W. S. et al. High-performance photovoltaic perovskite layers fabricated through intramolecular exchange. *Science* **348**, 1234–1237 (2015).
17. Lee, J.-W. et al. Tuning molecular interactions for highly reproducible and efficient formamidinium perovskite solar cells via adduct approach. *J. Am. Chem. Soc.* **140**, 6317–6324 (2018).
18. Kim, M. et al. Methylammonium chloride induces intermediate phase stabilization for efficient perovskite solar cells. *Joule* **3**, 2179–2192 (2019).
19. Jeong, J. et al. Pseudo-halide anion engineering for α-$FAPbI_3$ perovskite solar cells. *Nature* **592**, 381–385 (2021).
20. Lu, H. et al. Vapor-assisted deposition of highly efficient, stable black-phase $FAPbI_3$ perovskite solar cells. *Science* **370**, eabb8985 (2020).

21. Lee, J.-W., Kim, H.-S. & Park, N.-G. Lewis acid–base adduct approach for high efficiency perovskite solar cells. *Acc. Chem. Res.* **49**, 311–319 (2016).
22. Schottel, B. L., Chifotides, H. T. & Dunbar, K. R. Anion-π interactions. *Chem. Soc. Rev.* **37**, 68–83 (2008).
23. Sun, X. et al. Halide anion–fullerene π noncovalent interactions: n-doping and a halide anion migration mechanism in p–i–n perovskite solar cells. *J. Mater. Chem. A* **5**, 20720–20728 (2017).
24. Kan, C. et al. Mitigating ion migration by polyethylene glycol-modified fullerene for perovskite solar cells with enhanced stability. *ACS Energy Lett.* **6**, 3864–3872 (2021).
25. Garau, C. et al. Cation–π versus anion–π interactions: energetic, charge transfer, and aromatic aspects. *J. Phys. Chem. A* **108**, 9423–9427 (2004).
26. Anstöter, C. S., Rogers, J. P. & Verlet, J. R. R. Spectroscopic determination of an anion–π bond strength. *J. Am. Chem. Soc.* **141**, 6132–6135 (2019).
27. Stevenson, J. et al. Mayer bond order as a metric of complexation effectiveness in lead halide perovskite solutions. *Chem. Mater.* **29**, 2435–2444 (2017).
28. Shargaieva, O., Kuske, L., Rappich, J., Unger, E. & Nickel, N. H. Building blocks of hybrid perovskites: a photoluminescence study of lead-iodide solution species. *ChemPhysChem* **21**, 2327–2333 (2020).
29. Barrit, D. et al. Room-temperature partial conversion of α-$FAPbI_3$ perovskite phase via PbI_2 solvation enables high-performance solar cells. *Adv. Funct. Mater.* **30**, 1907442 (2020).
30. Zhang, H. et al. Bottom-up quasi-epitaxial growth of hybrid perovskite from solution process-achieving high-efficiency solar cells via template-guided crystallization. *Adv. Mater.* **33**, 2100009 (2021).
31. Stoumpos, C. C., Malliakas, C. D. & Kanatzidis, M. G. Semiconducting tin and lead iodide perovskites with organic cations: phase transitions, high mobilities, and near-infrared photoluminescent properties. *Inorg. Chem.* **52**, 9019–9038 (2013).

Methods

Materials

SnO_2 colloid precursor (tin(IV) oxide, 15% in H_2O colloidal dispersion), hydroiodic acid (HI, 57 wt% in water) and HFB was purchased from Alfa Aesar. Tin(II) chloride dihydrate (99.995%), thioglycolic acid, PbI_2 (99.999%), CsI (99.9%), N,N-dimethylformamide (99.9%), DMSO (99.5%), isopropanol (99.5%), chlorobenzene (99.8%), 4-tert-butylpyridine (98%) and acetonitrile (99.8%) was purchased from Sigma-Aldrich. Spiro-OMeTAD (99.8%), tris(2-(1H-pyrazol-1-yl)-4-tert-butylpyridine)-cobalt(III)tris(bis(trifluoromethylsulfonyl)imide) salt (FK209), poly[bis(4-phenyl)(2,4,6-trimethylphenyl)amine] (PTAA) was purchased from Xi'an Polymer Light Technology in China. Hydrochloric acid (HCl, 37 wt% in water) and methylamine water solution was purchased from Beijing Tongguang Fine Chemical Company. Formamidine acetate was purchased from MACKLIN. FTO substrate was purchased from Yingkou OPV Tech New Energy Co., Ltd.

Materials synthesis

MACl and FAI were synthesized using the methods reported previously. The details are as follows: 16 ml methylamine water solution (0.1 mol) or 8.8 g formamidine acetate (0.1 mol) was added to a 100-ml three-neck flask immersed in a water/ice bath. A certain amount (0.1 mol) of HX acid was slowly dropped into the bottle with continuous stirring. The mixture was refluxed for 2 h under a N_2 atmosphere. Subsequently, the solution was concentrated to a dry solid by using rotary evaporation at 80 °C. This crude product was redissolved into 20 ml ethanol, then 100 µl diethyl ether was slowly dropped along the bottle wall and a white product deposited. This recrystallization was repeated three times and the obtained precipitate was dried in a vacuum oven for 10 h at 40 °C. The final products were sealed in a N_2-filled glovebox for future use.

Solar cell device fabrication

The FTO or ITO substrate was cleaned with ultrapure water, acetone, ethanol and isopropanol successively. For highly efficient PSCs, SnO_2 was deposited in a chemical bath, similar to a previous report[32], and annealed at 150 °C for 60 min in air. For the stability test, a SnO_2 nanocrystal solution was spin-coated on the ITO substrate at 4,000 r.p.m. for 30 s to form a 50-nm-thick film, which was then annealed at 150 °C for 60 min in air. The perovskite film was fabricated by a two-step solution process: the PbI_2 (1.5 M, dissolved in DMF/DMSO (9:1, v/v)) was spin-coated on SnO_2 at 1,500 r.p.m. for 30 s. Organic cation solution (FAI 0.55 M; MACl 0.12 M) was spin-coated at 2,100 r.p.m. for 30 s and then annealed at 170 °C for 10 min in a dehumidified box (RH < 30%). The organic cation was dissolved in isopropanol for reference perovskite or a mixture of isopropanol/HFB (945:55, 890:110, 835:165 and 780:220, v/v for 1HFB, 2HFB, 3HFB and 4HFB, as optimized in Supplementary Fig. 16) for HFB-treated perovskite. Phenylethanamine salt (20 mM) was spin-coated onto the perovskite films at 3,000 r.p.m. for 30 s. Then the HTM solution, in which a spiro-OMeTAD/chlorobenzene (72.3 mg ml^{-1}) solution was used with the addition of 35 µl Li-TFSI/acetonitrile (260 mg ml^{-1}) and 30 µl 4-tert-butylpyridine, was deposited by spin-coating at 3,500 r.p.m. for 30 s. The device was finished by thermal evaporation of Au (80 nm) under vacuum. For the operational stability test inside the glovebox, a further 7 µl FK209 (0.55 M in acetonitrile) and 7 mg PTAA was added to 1 ml of the HTM solution to prevent possible dedope and deposited at 2,000 r.p.m. For the thermal stability test, 15 mg PTAA with the addition of 7.5 µl Li-TFSI/acetonitrile (180 mg ml^{-1}) and 10 µl 4-tert-butylpyridine was deposited by spin-coating at 3,000 r.p.m. for 30 s.

Basic material characterization

The morphology of perovskite films was measured using a cold field-emission scanning electron microscope (Hitachi S-4800). The XRD patterns were collected using a PANalytical X'Pert Pro X-ray powder diffractometer with Cu Kα radiation ($\lambda = 1.54050$ Å). PL was measured by a FLS980 fluorescence spectrometer (Edinburgh Instruments Ltd.) with an excitation at 450–470 nm. Time-resolved PL was measured by the FLS980 fluorescence spectrometer with excitation wavelength at 470 nm. The UV–vis absorption spectra were obtained using an UV–vis diffuse reflectance spectrophotometer (Hitachi UH4150). In situ UV–vis absorption spectra were tested by reacting the as-prepared PbI_2 films and organic cation solutions in a Quartz Flow-Through Semi-Micro Cuvette with a 2-mm slit. XPS measurements were carried out on an XPS AXIS Ultra DLD (Kratos Analytical). The current density–voltage characteristics of the perovskite devices were obtained using a Keithley 2420 Source Measure Unit under AM 1.5 G illumination at 1,000 W m^{-2} with a Newport Thermal Oriel 91192 solar simulator. The shading mask and one of our best devices were sent to the NIM for certification. The active area was defined as 0.0831 cm^2. EQEs were measured by an Enlitech EQE measurement system. PL mapping was measured by a laser scanning confocal microscope (Enlitech, SPCM-1000) equipped with a 470-nm pulse laser and galvo-based scanner in air, in which the signal of area 1,225 (35 × 35) µm^2 was collected. Thermal gravimetric analysis was obtained from a SDT Q600 thermogravimetric analyser (TA Instruments) with a ramping at 30 °C min^{-1} from 20 °C to 180 °C. For sample preparation, 100 µl of different organic cation solutions was spin-coated onto the as-prepared PbI_2 films for 10 s at 20 °C. Then the whole films were scraped from the substrate and transferred to the measurement furnaces immediately. FTIR was measured by a Spectrum Spotlight 200 FTIR microscope. Time-of-flight SIMS measurement was performed using a PHI nanoTOF II instrument (ULVAC-PHI, Inc.). A 30-keV Bi$^+$ pulsed primary ion beam was used for the analysis. TEM and the electron diffraction test were taken in an aberration-corrected JEOL JEM-ARM300F microscope at 300 KV. The precursor used for preparing the TEM sample was one-fifth of the concentration used for devices, which is suitable for TEM measurement. The structure optimization and electrostatic potential of HFB–FAI was estimated by the DFT calculation using the Gaussian 16 software package[33]. To carefully consider the weak intermolecular interaction of the complex, the DFT calculations were carried out with the DFT functional ωB9X-D (ref. 34) and basis set Def2TZVP. The electrostatic surface potential of the complex was generated with GaussView software. Films for the phase stability test were aged in a box with a humidifier. The operational stability was tested under an AM 1.5 G solar system (WAVELABS SINUS-70), in which the devices were loaded into an electrochemical workstation (CHI1000C, CH Instruments) and the loading voltage was fixed at MPP manually. During the operational stability test, the device temperature is measured to be 50 ± 5 °C.

QCM-D monitoring

QCM-D measurements were performed in the QSense Analyzer (Biolin Scientific). PbI_2 was deposited on quartz sensors coated with silicon dioxide using the same method as the devices. FAI/IPA or FAI/HFB + IPA solutions were pumped into a chamber continuously and reacted with PbI_2. Changes in the frequency of the third, fifth, seventh and ninth overtones ($n = 3, 5, 7, 9$) are used to fit mass change in the Kelvin–Voigt model.

ICP-AES test

The inductively coupled plasma atomic emission spectroscopy (ICP-AES) test was taken in the Prodigy7 ICP-OES (Teledyne Leeman Labs). In our experiment, PbI_2 films were coated on a glass slide by doctor blade coating, which was placed vertically and reacted with 70 ml FAI/IPA or FAI/HFB + IPA solutions (2 mg ml^{-1} for FAI) in a glass container. The container vial was sealed to prevent evaporation of the solvent so that the mass of FAI could not be overestimated owing to solvent evaporation. After a certain reaction time as reported in the manuscript (15 s, 30 s, 60 s, 120 s, 1,200 s, 3,600 s), the glass slide with

PbI_2 film was removed immediately from the reaction container and the FAI solution was stirred evenly. Then the solution was extracted and diluted (1:39 v/v) in water before sending to test. An extra 50 mg ml^{-1} of sodium hypophosphite was added to prevent oxidation and evaporation of iodine.

Data availability

All data are available in the main text or the supplementary information.

Code availability

The code used for this study is available from the corresponding authors on reasonable request.

32. Yoo, J. J. et al. Efficient perovskite solar cells via improved carrier management. *Nature* **590**, 587–593 (2021).
33. Gaussian 16, Revision C.01 (Gaussian, Inc., 2016).
34. Salzner, U. & Aydin, A. Improved prediction of properties of π-conjugated oligomers with range-separated hybrid density functionals. *J. Chem. Theory Comput.* **7**, 2568–2583 (2011).
35. Guha, S., Goodson, F. S., Corson, L. J. & Saha, S. Boundaries of anion/naphthalenediimide interactions: from anion–π interactions to anion-induced charge-transfer and electron-transfer phenomena. *J. Am. Chem. Soc.* **134**, 13679–13691 (2012).
36. Giese, M., Albrecht, M. & Rissanen, K. Anion−π interactions with fluoroarenes. *Chem. Rev.* **115**, 8867–8895 (2015).

Acknowledgements This work was supported by the National Natural Science Foundation of China (grant nos. 52125206, 51972004 and 52202241), the National Key Research and Development Program of China (grant no. 2020YFB1506400) and the Tencent Foundation through the Xplorer Prize. We would like to thank the staff at beamlines BL14B1 and BL11B at the Shanghai Synchrotron Radiation Facility (SSRF) for their help with GIWAXS and EXAFS characterizations, and H. Zhengguan (SSRF) for designing the in situ GIWAXS measurement. We acknowledge Y. Chen (Peking University) for the discussion on DFT calculations, Y. Jiang (Peking University) for the assistance in designing *C*–*V* measurement and C. Zhu (Beijing Institute of Technology) for the assistance with the material structure analysis. We acknowledge support from T. Yang (Jiangnan University) for the help with the GIWAXS test and L. Xiong and Z. Yan (Jiangnan University) for the help with the QCM-D test.

Author contributions Z.H. and H.Zhou conceived the idea and designed the experiments. Z.H. fabricated and characterized the perovskite films. Z.H. and Y.B. fabricated the solar cell devices. Y.W. ensured device encapsulation and preservation and participates in efficiency certification. Y.B. performed the SIMS mapping test. X.H. and L.W. performed the TEM measurement. J.L. and T.L. performed and helped to analyse the DFT calculations. Y.C. helped with the scheme design. K.L. performed the SEM measurements. X.N. conducted the XPS, EQE and PL mapping measurements. N.L. carried out the FTIR measurements. Y.Z. and H.Zai contributed to the fabrication of high-performance PSCs. H.Zhou, Q.C. and Z.H. wrote and revised the manuscript. All authors were involved in the discussion of data analysis and commented on the manuscript.

Competing interests The authors declare no competing interests.

Additional information

Supplementary information The online version contains supplementary material available at https://doi.org/10.1038/s41586-023-06637-w.

Correspondence and requests for materials should be addressed to Huanping Zhou.

Peer review information *Nature* thanks the anonymous reviewers for their contribution to the peer review of this work.

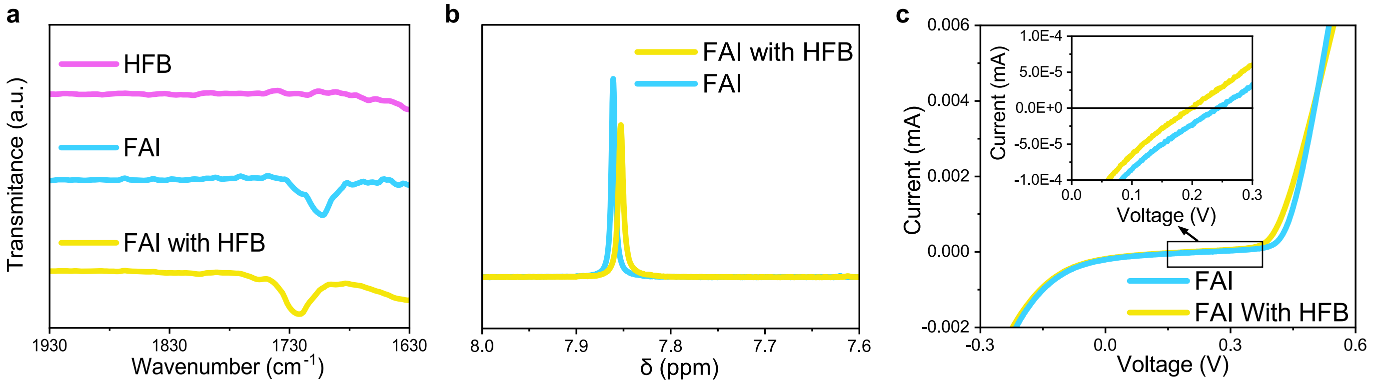

Extended Data Fig. 1 | Interaction between FAI and HFB. a, FTIR spectra of FAI, HFB or mixed FAI and HFB. **b**, ^{1}H NMR of FAI and FAI with HFB in DMSO-d_6. **c**, *C*–*V* measurement of iodine ion activity of FAI or FAI with HFB. The electrode oxidation potential E_{I^-} of FAI (0.2 mg ml^{-1}) in IPA at 293 K is +0.245 V, which dropped to +0.197 V of FAI with the addition of HFB ($E_{I^- -\mathrm{HFB}}$). The activity of iodide without (γ_{I^-}) and with ($\gamma_{I^- -\mathrm{HFB}}$) HFB could be compared using the Nernst equation $E_{I^-} - E_{I^- -\mathrm{HFB}} = RT\ln(\gamma_{I^-}/\gamma_{I^- -\mathrm{HFB}})/F$. The $\gamma_{I^-}/\gamma_{I^- -\mathrm{HFB}}$ ratio is determined to be 2.2, indicating the substantially reduced activity of iodide ions. The decrease in the ion activity ultimately leads to a decrease in the chemical potential of FAI, which retards the reaction between FAI and PbI_2.

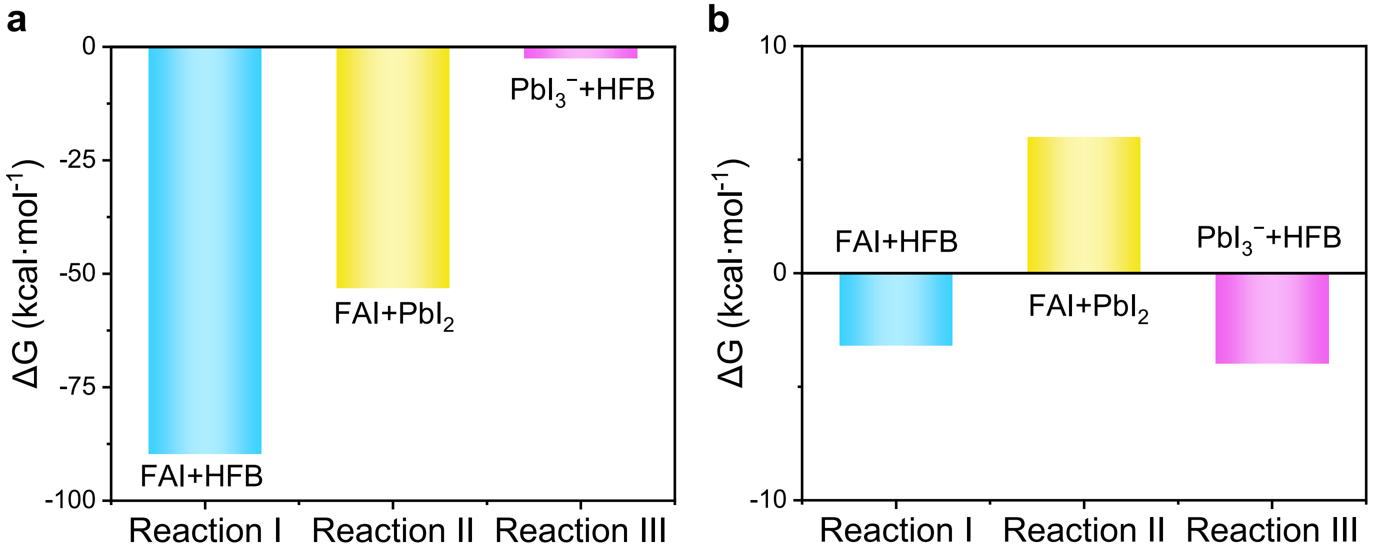

Extended Data Fig. 2 | DFT calculations for the FAI···HFB···PbI_2 three-component system. DFT-calculated Gibbs energy of three reactions in gas phase (**a**) and the implicit solvent model (solvent = DMF) (**b**). According to the implicit solvent model, we observed that the Gibbs energy of reaction 1 (−3.19 kcal mol^{-1}) is still lower than that of reaction 2 (6.00 kcal mol^{-1}) in solvent. Notably, reaction 3 ($\Delta G = -3.97$ kcal mol^{-1}) became more favourable in solvent, which is consistent with the UV–vis absorption spectra of the three-component system (Fig. 1d). This was probably because of the coordination of solvent molecules in the implicit solvent model. But the energy of reaction 3 in solvent is still not enough to cancel out the energy difference between reaction 1 and reaction 2. Therefore, DFT calculations in gas phase as well as in the implicit solvent model (solvent = DMF) yield consistent results, that HFB reacts with FAI to form [FAI···HFB] and retards the reaction between FAI and PbI_2.

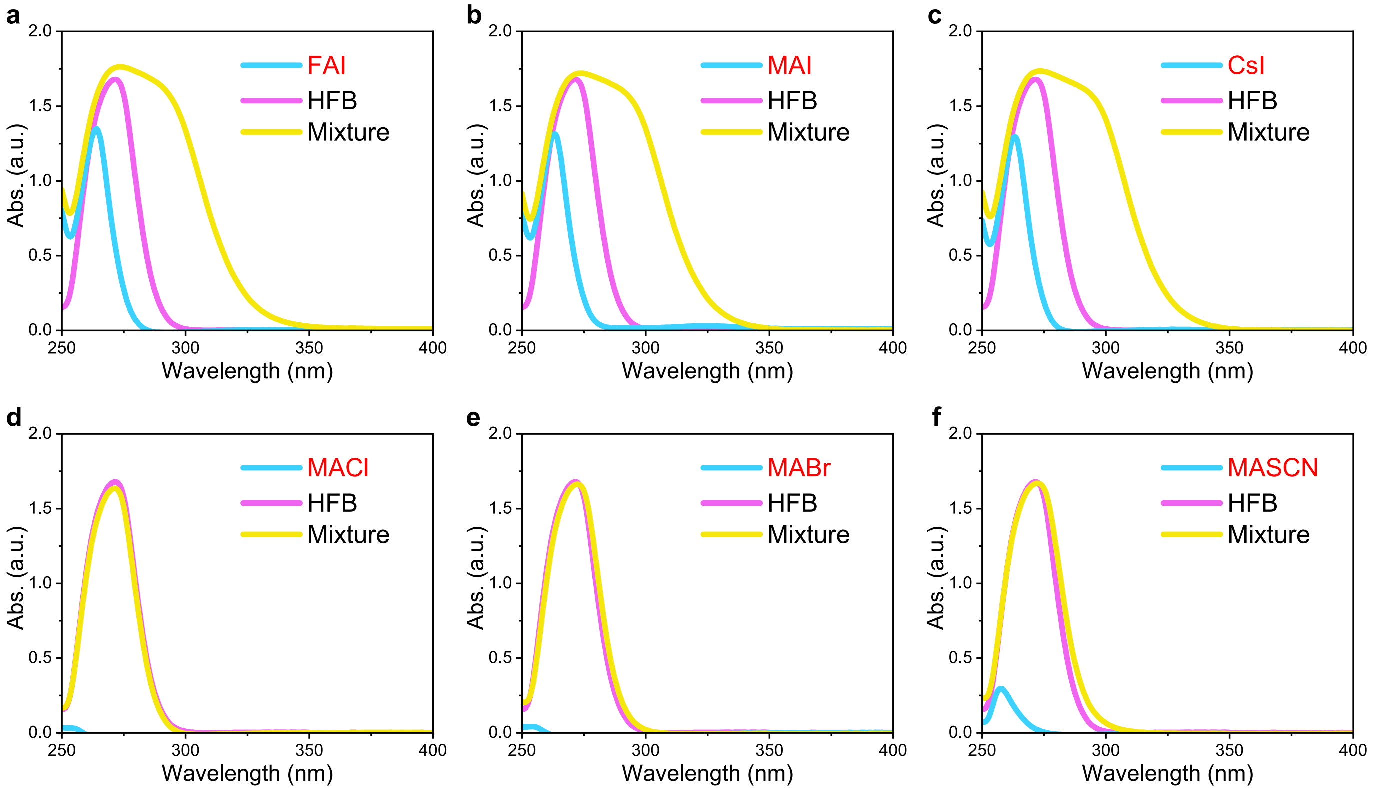

Extended Data Fig. 3 | Anion–π interaction between the AX component of perovskite and HFB. UV–vis absorption spectra for HFB, various salts with different cations and anions FAI (**a**), MAI (**b**), CsI (**c**), MACl (**d**), MABr (**e**), MASCN (**f**) and their mixture. Similar redshift about the absorption edge from 280 nm to more than 320 nm was found after FAI, MAI or CsI solution mixing with HFB, indicating that this polarization appeared regardless of the cation species[35]. Besides, the absorption edge of HFB at 280 nm shifted to 285 nm and 300 nm after mixing with Br^- and SCN^-, respectively. These evidences implied that such polarization also existed between HFB and bromide or even SCN^-. It should be noted that there is no redshift observed when HFB is mixed with chloride, indicative of no polarization, which is probably because of the small radius of chlorine. However, because anion–π interactions also consisted of the contribution from electrostatic force, the strong electrostatic force between Cl^- and HFB also leads to anion–π interactions, as reported previously[36]. These results indicate that the anion–π interaction is widely present between HFB and various types of AX in perovskite.

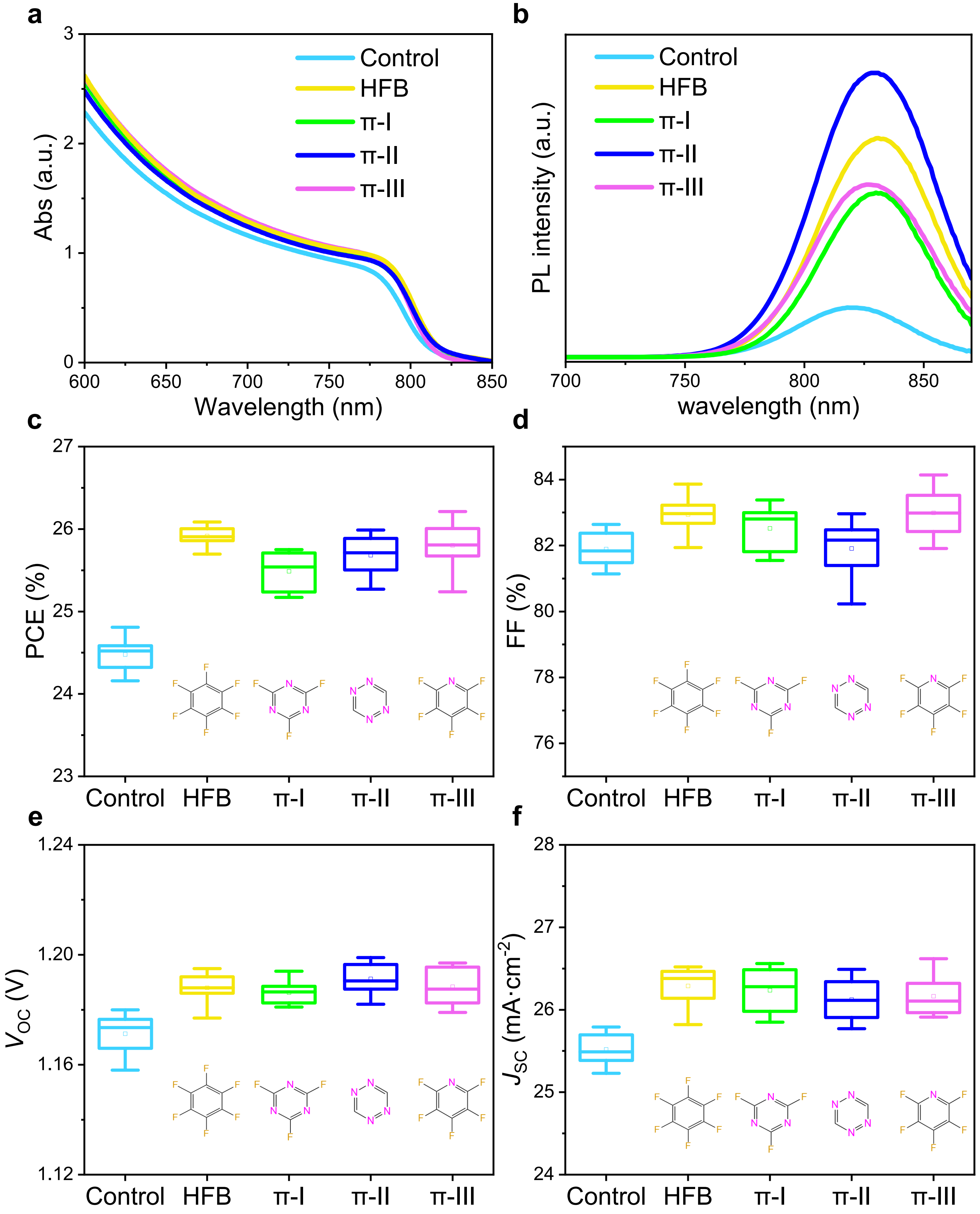

Extended Data Fig. 4 | Effects of other strong electron-deficient molecules. UV–vis absorption (**a**) and PL spectra (**b**) of control perovskite and perovskite fabricated with HFB, 2,4,6-trifluoro-1,3,5-triazine (labelled π-I), s-tetrazine (labelled π-II) and pentafluoropyridine (labelled π-III). PCE (**c**), FF (**d**), V_{OC} (**e**) and J_{SC} (**f**) of PSCs fabricated with HFB, π-I, π-II and π-III.

Extended Data Table 1 | Summarized characteristics of PSCs

Device	Scan Direction	V_{OC} (V)	J_{SC} (mA cm^{-2})	FF (%)	PCE (%)
HFB	Reverse	1.191	26.39	82.94	26.07
	Forward	1.187	26.37	83.09	26.01
control	Reverse	1.176	25.85	81.59	24.81
	Forward	1.154	25.84	79.76	23.78